

# PCCP

Accepted Manuscript



This is an *Accepted Manuscript*, which has been through the Royal Society of Chemistry peer review process and has been accepted for publication.

*Accepted Manuscripts* are published online shortly after acceptance, before technical editing, formatting and proof reading. Using this free service, authors can make their results available to the community, in citable form, before we publish the edited article. We will replace this *Accepted Manuscript* with the edited and formatted *Advance Article* as soon as it is available.

You can find more information about *Accepted Manuscripts* in the [Information for Authors](#).

Please note that technical editing may introduce minor changes to the text and/or graphics, which may alter content. The journal's standard [Terms & Conditions](#) and the [Ethical guidelines](#) still apply. In no event shall the Royal Society of Chemistry be held responsible for any errors or omissions in this *Accepted Manuscript* or any consequences arising from the use of any information it contains.

# Controllable synthesis of 3D BiVO<sub>4</sub> superstructure with visible-light-induced photocatalytic oxidation of NO in gas phase and mechanism analysis

Man Ou, Haoyu Nie, Qin Zhong\*, Shule Zhang, Lei Zhong

*School of Chemical Engineering, Nanjing University of Science and Technology, Nanjing, Jiangsu*

*210094, P.R. of China*

*Nanjing AIREP Environmental Protection Technology Co., Ltd,*

*Nanjing, Jiangsu210091, P.R. of China*

*\*Corresponding author: Qin Zhong.*

*Email: zq304@mail.njust.edu.cn. Tel/Fax number: +86 25 84315517.*

## Abstract

A surfactant-free solvothermal method was developed for the controlled synthesis of diverse 3D ms-BiVO<sub>4</sub> superstructure, including flower, double-layer half-open flower and hollow tube with square cross-sections, via facilely adjusting the pH values with the aid of NH<sub>3</sub>·H<sub>2</sub>O. The effects of the morphologies of the prepared 3D ms-BiVO<sub>4</sub> superstructure on the photocatalytic oxidation of NO was investigated, indicating that the enhanced photoactivity was not related to the surface area, but associated with the unique morphology, surface structure and good crystallinity. Moreover, the flower-like ms-BiVO<sub>4</sub> photocatalyst with more (040) reactive crystal plane exhibited higher photoactivity than those of other samples. The unique morphology helped with flushing the oxidation products accumulated on the surface of photocatalysts in the H<sub>2</sub>O<sub>2</sub> system, and further improved the photoactivity. A trapping experiment was also conducted to examine the effects of the active species involved in the PCO of NO intuitively.

**Keywords:** visible-light; ms-BiVO<sub>4</sub>; PCO; morphologies; active species

## 1 introduction

Recently, semiconductor photocatalysts on the microstructure-dependent properties has been a focus of interest due to the strong connection between their structural properties and photocatalytic performance.<sup>1-3</sup> Particularly, the self-assembly of one-dimensional (1D) nanostructures into three-dimensional (3D) superstructures has attracted great concerns due to its unique morphology and surface structure. The conversion of photoelectron or photocatalytic reaction could take place only when photoinduced electrons and holes are available on the surface of photocatalysts.<sup>4</sup> Therefore, the surface structure of photocatalysts is greatly related to their photocatalytic performance. In addition, considerable experiments also demonstrated that the photocatalytic activity of a photocatalyst was strongly dependent on its morphology and crystallinity.<sup>5,6</sup> Therefore, fabricating highly visible-light-active photocatalysts with controlled 3D superstructure is necessary.

$\text{BiVO}_4$ , a common and significant visible-light (VL) photocatalytic material, has drawn enormous attention of researchers in the photocatalytic field due to its relatively small band gap of 2.4 eV, which enables efficient light adsorption and easily to be stimulated to produce the photogenerated charge carriers.<sup>7,8</sup> It has been used for a wide range of applications as a promising photocatalyst for water splitting to oxygen, harmful pollutants decomposing and NO degradation under visible-light irradiation.<sup>9-13</sup>  $\text{BiVO}_4$  mainly exists in three crystalline phases: tetragonal zircon structure (tz- $\text{BiVO}_4$ ), monoclinic scheelite structure (ms- $\text{BiVO}_4$ ) and tetragonal scheelite structure (ts-  $\text{BiVO}_4$ ), among which ms- $\text{BiVO}_4$  is found to exhibit far better visible-light-driven photocatalytic activity over other crystal forms.<sup>14,15</sup> In the past decades, many researchers made great efforts in studies of the relationship between the photocatalytic performance and relevant influencing factors, including the morphology, crystallinity, specific surface area and the surface structure. Sun et al. proposed the synthesis of diverse 3D ms- $\text{BiVO}_4$  hierarchical structure via a mixed solution hydrothermal route, and demonstrated that the enhanced photocatalytic activity was only associated with the unique morphology.<sup>16</sup> The Sheet-like  $\text{BiVO}_4$  material, displaying a preferred (040) surface orientation using  $\text{TiCl}_3$  as the directing agent, demonstrated higher

visible-light photocatalytic activity for  $O_2$  evolution.<sup>17</sup> Kudo assumed that good crystallinity provides a significant effect on the photocatalytic performance of  $O_2$  evolution under visible light irradiation.<sup>6</sup> Considering that photocatalytic properties are closely associated with the microstructure, it is of great importance to study the controllable preparation of ms-BiVO<sub>4</sub> with desired morphology and surface structure.

Herein, we reported a surfactant-free solvothermal method, from which single crystals ms-BiVO<sub>4</sub> with controlled morphology could be obtained by facilely changing the pH values. The evolution process of 3D ms-BiVO<sub>4</sub> superstructures via altering the pH of the precursor solution was fully explored. In the study, experiments of photocatalytic oxidation (PCO) of NO were conducted with a high concentration of NO (~ 400 ppm) in gas phase and the final product was NO<sub>3</sub><sup>-</sup> in VL/ms-BiVO<sub>4</sub>/H<sub>2</sub>O<sub>2</sub> system. Moreover, the relationship between the further PCO of NO and related influencing factors, involving the surface area, crystallinity, the surface structure as well as the morphology was clarified. This study also focused on the understanding of the influence of the morphology on the dispersion of oxidation products and the identification of the main active species in the PCO of NO process in an intuitive way.

## 2 Experimental section

### 2.1 Synthesis of the photocatalyst

The 3D BiVO<sub>4</sub> superstructure was synthesized by a solvothermal method: 1.940 g Bi(NO<sub>3</sub>)<sub>3</sub>·5H<sub>2</sub>O was dissolved in 40 mL ethylene glycol (EG) solution and then the solution was stirred for 30 min at room temperature to obtain colorless transparent sticky solution, marked as solution A. Meanwhile, 0.468 g NH<sub>4</sub>VO<sub>3</sub> was dissolved in 40 mL 80 °C distilled water with mechanical agitation until the dissolution was completed, and the resultant solution was marked as solution B. Then solution B was added dropwise into solution A to form a salmon suspension (pH ~ 2) under continuously magnetic stirring. After stirring for 30 min, NH<sub>3</sub>·H<sub>2</sub>O was added to adjust the pH value, and the yellow precipitation was formed immediately. The precursor solution was

consequently transferred into a 100 mL Teflon-lined stainless steel autoclave and maintained at 100 °C and autogenous pressure for 15 h. After the autoclave was cooled down to room temperature, the luminous yellow precipitation was collected by centrifugation, washed by distilled water and absolute alcohol for several times, and then dried at 90 °C overnight.

## 2.2 Characterization

X-ray diffraction (XRD) patterns were recorded on a Beijing Purkinjie general instrument XD-3 X-ray diffraction (Cu K $\alpha$ , voltage 36 kV, electrical current 20 mA). Field-emission scanning electron microscope (SEM) observations were carried out using a FEI Quanta 250F. Transmission electron microscope (TEM) observations were carried out using a Philips CM-10 at 80 kV and a CM-12 at 120 kV. X-ray photoelectron spectroscopy (XPS) was performed on a RBD upgraded PHI-5000C ESCA system (Perkin-Elmer) with Mg K $\alpha$  radiation ( $h\nu = 1253.6$  eV). The UV-vis diffuse reflectance spectra (DRS) were performed on a Shimadzu UV-2600 UV-vis spectrophotometer using BaSO<sub>4</sub> as the reference sample.

## 2.3 Detection of hydroxyl radicals

The formation of hydroxyl radicals ( $\cdot\text{OH}$ ) in the VL/ms-BiVO<sub>4</sub>/H<sub>2</sub>O<sub>2</sub> system was detected by the fluorescence technique using terephthalic acid (TA) as a probe molecular. The brief experimental procedures were as follows: two quartz tubes, filled with 40 mL aqueous solution containing 0.3 mmol TA and 50  $\mu\text{L}$  30% H<sub>2</sub>O<sub>2</sub> solution at room temperature, were divided into the experimental group and the control group. Then 10 mg ms-BiVO<sub>4</sub> (pH 8) was dispersed into the experimental group. Subsequently, both tubes were put under visible-light irradiation in stirring condition for 120 min. After the clear supernatant was obtained by centrifugation (5000 rpm, 5 min),  $\cdot\text{OH}$  in the solution was measured by a FL3-TCSPEC fluorescence spectrophotometer.

## 2.4 Photocatalytic reaction

Initially, 0.2 g grinded powder of the photocatalyst was carefully tiled on the inner wall of the tubular quartz reactor ( $d = 1$  cm,  $h = 15$  cm), then 0.5 mL deionized water was dropped on the photocatalyst powder to form a thin layer of immobilized photocatalyst. After deposition, the reactor was dried at  $100^\circ\text{C}$  overnight to remove the water and retain the photocatalyst powder fixed on the inner wall. Also, a small piece of clean cotton was placed at the bottom of the reactor. After the PCO of NO experiments, few  $\text{BiVO}_4$  photocatalyst was found on the cotton, which demonstrated that the layer of the photocatalyst had a desirable resistance to the air flow and the small flow of the  $\text{H}_2\text{O}_2$  solution.

The PCO of NO was carried out at room temperature and atmospheric pressure by the setup consisting of a fixed bed continuous flow reactor connected to the gas delivery system and analytical system, as shown in Figure 1. The artificial coal-fired power plant flue gas,  $\text{N}_2$  gas,  $\text{O}_2$  gas and 1% NO in  $\text{N}_2$  from the cylinders were mixed using mass flowmeter to obtain the reactant gases concentration (400 ppm NO, 7 vol.%  $\text{O}_2$  and  $\text{N}_2$  balance) and total flow rate of 100 mL/min. The 350 W Xe lamp was vertically placed, parallel with the reactor and a 420 nm cut-off filter was also placed. In order to reduce the accumulation of reaction products on the surface of the catalyst and provide more active species, 30%  $\text{H}_2\text{O}_2$  solution was injected into the reactor by a peristaltic pump with a flow rate of 0.04 mL/min. After the system achieved the stable state for 60 min, when there was no difference between outlet NO concentration and that of inlet gas, the peristaltic pump and Xe lamp were turned on and then the experiment started. The gas products (every 10 min reaction) were analyzed by an Ecom-JZKN flue gas analyzer (Germany) for 150 min under visible-light irradiation. The liquid products scoured by  $\text{H}_2\text{O}_2$  were collected in a 10 mL volumetric flask. The NO conversion was defined as:

$$\text{NO conversion} = \frac{\text{NO}_{in} - \text{NO}_{out}}{\text{NO}_{in}} \times 100\%$$

(Figure 1)

### 3 Results and discussion

### 3.1 XRD analysis of the BiVO<sub>4</sub> powders

Figure 2 shows the XRD patterns of BiVO<sub>4</sub> powder prepared at different pH values. The synthesis at acidic or neutral condition (pH = 2 or 7) led to a mixture of scheelite BiVO<sub>4</sub> structure in tetragonal (JCPDS No. 14-0133) and monoclinic (JCPDS No. 14-0688) phase (Fig 2a).<sup>18,19</sup> On the contrary, samples prepared at alkaline condition (pH = 8, 9 and 10) only presented the pure phase with monoclinic structure, as shown in Fig 2b. It is noticeable that NH<sub>3</sub>·H<sub>2</sub>O was crucial in forming the monoclinic BiVO<sub>4</sub>. Although the monoclinic BiVO<sub>4</sub> was thermodynamically more stable, the tetragonal phase was kinetically more feasible by a sudden increase of pH by adding NH<sub>3</sub>·H<sub>2</sub>O.<sup>20</sup> As a mineralizer, NH<sub>3</sub>·H<sub>2</sub>O facilitated the generation of tetragonal structure at the first stage and subsequently transformed to monoclinic phase via a dissolution-recrystallization process.<sup>21</sup> Therefore, with the further increase of added NH<sub>3</sub>·H<sub>2</sub>O, pure monoclinic BiVO<sub>4</sub> was preferable to be generated during the recrystallization process. The pH value of the EG solution reduced from 5.83 to 2.56 after the adding of Bi(NO<sub>3</sub>)<sub>3</sub>·5H<sub>2</sub>O, suggesting that Bi<sup>3+</sup> reacts with EG to form soluble BiY<sup>+</sup> and H<sup>+</sup> species. Subsequently the BiVO<sub>4</sub> crystal nucleus were obtained (as shown by reactions 3-1 and 3-2):



EG is assigned as H<sub>2</sub>Y. From pH 8 to pH 10, the H<sup>+</sup> species were consumed gradually as the pH values constantly increased, which induced the reaction equilibrium to the positive direction. Therefore, all the tetragonal phase was forced to transfer to the monoclinic phase in this pH region. The similar results had been reported by Tan et al.<sup>21</sup> In addition, NH<sub>3</sub>·H<sub>2</sub>O, as a buffer, served as the rate-determining factor in controlling the concentration of the BiVO<sub>4</sub> monomer in the bulk solution to adjust the nucleation rate and crystal growth rate of BiVO<sub>4</sub>.<sup>22</sup> The BiVO<sub>4</sub> crystals grew along different crystal plane at different growth rates. It is worth noting that the relative intensity of the diffraction peaks (I<sub>040</sub>/I<sub>121</sub>) shrank notably, and at the same time the diffraction peaks

corresponding to  $I_{110}/I_{121}$  and  $I_{002}/I_{121}$  notably rose up as the pH value increased (Table 1). This would denote a change in morphology. In addition, a relatively good crystallization was obtained at pH = 8 with respect to the remaining two samples. The XRD analysis indicated that: (1) it was favorable for the formation of pure monoclinic  $\text{BiVO}_4$  at higher pH, which displayed a higher VL photocatalytic activity as compared to zircon structure with tetragonal phase and sheetlike structures with tetragonal phase. (2) The concentration of  $\text{OH}^-$  was relevant with the crystallinity and the preferential orientation of the lattice plane, which played a significant role in the formation of the morphologies of 3D  $\text{BiVO}_4$  superstructure.

(Figure 2)

### 3.2 Morphology characterization

The morphology and microstructures of ms- $\text{BiVO}_4$  synthesized at different pH values were revealed by SEM, which were shown in Fig. 3. From the SEM images, it could be seen that the morphology of ms- $\text{BiVO}_4$  was dramatically affected by the pH values of the precursor solution. The panoramic view shown in Fig 3a<sub>1</sub> clearly demonstrated that the synthesized particles at pH 8 were almost entirely blooming flower-like with a uniform size of distribution, and possessed relatively sharp facets and edges. Close investigation of the samples through the high magnification images in Fig 3a<sub>2</sub> showed that the whole flower displayed a 3D eight-pot-shaped structure with high symmetry, which was confirmed by the clear axial lines of the petals. In addition, as shown in Fig 3a<sub>3</sub>, a single framework was composed of a number of small smooth slices that were closely attached one by one, and then to form the unique premature flower-like structure. This premature morphology revealed that  $\text{BiVO}_4$  particles self-assembled along the eight  $\langle 111 \rangle$  directions of the cube lattice. And simultaneously in situ growth of the particles perpendicular to the self-assembled plane led the formation of the framework composed of the slice-like structure. Finally, as the reaction proceeded, the open space between the pots was gradually filled with the slices, and finally the mature 3D ms- $\text{BiVO}_4$  superstructure was obtained. The schematic illustration is shown

in Fig 4. The results of the formation and evolution process of the similar flower-like structure had been reported by Wang et al.<sup>23</sup> With the increase of the pH value of the precursor solution up to 9, a well-defined double-layer half-open flower morphology was obtained (Fig 3b<sub>1</sub>). All flowers which were not full and huddled together had a similar structure, and they were also evenly distributed. The magnification images in Fig 3b<sub>2</sub> in which the eight-pot-shaped structure was also formed, indicated that the particles aggregated along the eight  $\langle 111 \rangle$  directions of the cubic lattice. Furthermore, perpendicular to the aggregated plane, a single framework was composed of many parallel aligned rods and the rods were connected with each other end to end. Similarly, it could be suggested that the particles self-assembled into initial eight-pot-shaped morphology and they were perpendicular to the self-assembled plane in situ growth of the particles to form the rod-like structure. Finally, as the reaction progressed, the open space between the pots was gradually filled with the parallel end-to-end linked rods and constructed a well-fined double-layer half-open flower hierarchical structure. Finally, after tuning the pH value to 10, a hollow tube with square cross-sections was fabricated as shown in Fig 3c<sub>1</sub>. This structure seemed to be contracted compared with the half-open flower structure at pH 9. Close observation in Fig 3c<sub>2</sub> that the tube was bound tightly by several long strips. Based on above results, it suggested that the subunits changed from slices to rods and then to strips with the increase of the pH value.

The crystals grew along the different directions at different growth rates. As the reaction proceeded, the crystal plane with the higher growth rate would disappear first, while the crystal plane with the lower growth rate would increase in area and then exposed on the surface of the crystals. The XRD intensity of the crystal facet was positively correlated with the area of corresponding crystal facet.<sup>21</sup> Therefore, the differences in the morphology caused by the change of crystal plane could be associated with the evolution in the XRD pattern. As the gradual increase of the pH up to 10, the relative intensity of the (040) diffraction peak became distinctly weaker and the (110) and (002) diffraction peak became obviously stronger. Therefore, the (040) plane displayed

a higher growth rate and a lower crystal area while the (110) and (002) planes exhibited a lower growth rate and an increased crystal area with the increase of pH values. It is obvious that the variation of these crystal planes caused the difference of the subunits at different conditions. The exaltation of the (110) and (002) crystal planes and the extinction of (040) crystal plane induced the subunits to elongated along the (110) and (002) planes,<sup>24</sup> as shown in Fig. S1. Therefore, the subunit structure varied from slice to strip. With the increase of the pH, the morphology of ms-BiVO<sub>4</sub> particles varied from flower-like to tubular shape with the transition state of half-open flower-like structure. This morphology evolution during changing the pH indicated that the synthesis was somewhat like a reverse process of flower in full bloom.

**(Figure 3)**

**(Figure 4)**

To further confirm the evolution of the shape, the transmission electron microscopy (TEM) images were recorded and shown in Fig 5. The shapes of these samples were in accordance with the SEM observation. The HRTEM images were taken on the edge of the subunit in each ms-BiVO<sub>4</sub> (Fig 5a<sub>1</sub>, b<sub>1</sub> and c<sub>1</sub>) at different pH values. And the corresponding selected area electron diffraction (SAED) was shown in the inset. Well-developed lattice fringes can be clearly seen (Fig 5a<sub>2</sub>, b<sub>2</sub> and c<sub>2</sub>), conforming that these ms-BiVO<sub>4</sub> samples were of good crystallinity and single crystalline nature of the subunits. The fringe spacing of 0.475 nm corresponding to the (110) lattice plane of the ms-BiVO<sub>4</sub> sample was clearly seen in all samples, which was consistent with the results of XRD patterns. It was illustrated that the (110) plane ultimately became the preferential orientation at higher pH, agree with the previous work.<sup>24</sup> Results above presented that the morphology of ms-BiVO<sub>4</sub> systems was notably sensitive to the pH of the precursor solution. Base on the mechanism of morphology evolution, we could tune the morphology assembly, from the blooming flower-like to hollow tubular with square cross-sections by changing the pH value and without the use of any template or organic surfactant.

(Figure 5)

### 3.3 UV-vis absorption spectra analysis

UV-vis diffuse reflectance spectroscopy (DRS) was used to characterize the optical absorption property of the as-prepared samples. Fig. 6 shows the UV-vis absorption spectra of ms-BiVO<sub>4</sub> synthesized by varying the pH values. All samples exhibited adsorption bands in the VL region, the characteristic absorption pattern of ms-BiVO<sub>4</sub>.<sup>25</sup> However, a small effect of the pH was observed that the absorption edge of the ms-BiVO<sub>4</sub> red-shifted (i.e., shifted to higher wavelengths) with the increase of the pH. The band gap energies were, respectively, estimated from the intercept of the tangents to the plots of  $(\alpha h\nu)^2$  vs photon energy ( $h\nu$ ) to be 2.48 eV for ms-BiVO<sub>4</sub> (pH 8), 2.45 eV for ms-BiVO<sub>4</sub> (pH 9) and 2.44 eV for ms-BiVO<sub>4</sub> (pH 10). The optical band energy of ms-BiVO<sub>4</sub> was inversely collected with the photocatalytic performance (Part 3.5). Yu et al reported that quantum size effect, in which the crystal size was in the order of 1-10 nm, could lead to this abnormal trend.<sup>26</sup> However, it was easy to notice from the microscopic observations that the particles sizes of the ms-BiVO<sub>4</sub> sample were far beyond the region. Therefore, the observed trend could be suggested to be induced by the morphological changes of the ms-BiVO<sub>4</sub> samples. The same phenomenon was also found in experiments of Sun et al.<sup>16</sup> Interestingly, the ms-BiVO<sub>4</sub> (pH 8) exhibited a little stronger absorption in the VL region (250-470 nm) than others. As a consequence, the use of the ms-BiVO<sub>4</sub> (pH 8) as a promising photocatalyst was not affected by the small blue shift of the band gap.

(Figure 6)

### 3.4 XPS analysis

XPS was used to examine details in the variation of the ms-BiVO<sub>4</sub> sample in the PCO of NO reaction process. The ms-BiVO<sub>4</sub> (pH 8) sample was studied in three conditions: in the dark overnight (I), under visible light irradiation for 30 min (II) and after the end of 150 min PCO of NO experiment (III). The XPS profiles

corresponding to each element of  $\text{ms-BiVO}_4$  presented on the surface of samples where most catalytic and oxidative reactions are known to take place are shown in Fig. 7. The C 1s peak at 284.6 eV was used for calibration purpose. Two peaks of pure  $\text{ms-BiVO}_4$  (Fig. 7a) at 158.5 and 163.9 eV, assigned to Bi 4f<sub>7/2</sub> and Bi 4f<sub>5/2</sub> induced by Bi<sup>3+</sup> species,<sup>27</sup> were decreased to 158.7 and 164.0 eV under VL irradiation. Then the binding energy of Bi 4f at the end of photocatalytic reaction increased to 158.9 and 164.3 eV. The V 2p showed the peaks at 516.4 and 523.9 eV (Fig 7b), which were attributed to V<sup>5+</sup> of  $\text{ms-BiVO}_4$  particles.<sup>27,28</sup> Similarly, the peaks of V 2p also decreased under VL irradiation and then increased at the end of the PCO of NO experiment. The O 1s shown in Fig 7c could be unraveled into three peaks with binding energies of 529.5, 530.6 and 532.9 eV, corresponding to lattice oxygen, chemisorbed OH<sup>-</sup>, and physically adsorbed oxygen, respectively.<sup>29</sup> The variation tendency of lattice oxygen was consistent with Bi 4f and V 2p. It was obvious that the binding energies of each element of  $\text{ms-BiVO}_4$  photocatalyst decreased under VL irradiation, then increased after the photocatalytic experiment. It suggested that the electron density on the surface of  $\text{ms-BiVO}_4$  sample increased after VL irradiation, while decreased at the end of photocatalytic experiment. Furthermore, it was well known that the valance band edge was composed of Bi 6s and O 2p orbits, while the conduction band edge was contributed by V 3d orbit.<sup>30</sup> Results above illustrated that the valence-band electrons were excited to the conduction band and then transferred to the surface of the photocatalyst under VL irradiation, and subsequently consumed gradually in the photocatalytic reaction. The relative intensity of the chemisorbed OH<sup>-</sup> increased under VL irradiation, at which point it accounted for 40% of the total oxygen species and then declined to 17.5% after the end of the PCO experiment. The increase of OH<sup>-</sup> on the photocatalyst surface played an important role on the NO adsorption and oxidation process, thus increased the photocatalytic performance.<sup>31</sup> And OH<sup>-</sup> could be oxidized to ·OH by holes generated in the process of photocatalytic reaction, which could be the cause of the OH<sup>-</sup> decline.

**(Figure 7)**

### 3.5 Photocatalytic activity for NO oxidation and mechanism analysis

The VL driven photocatalytic oxidation efficiency of gaseous NO ( $\sim 400$  ppm) over the synthesized ms-BiVO<sub>4</sub> hierarchical structures at different pH values was investigated to basically evaluate the potential ability for the removal of NO in coal-fired flue gas. After the adsorption-desorption equilibrium between the gases with NO and photocatalyst was achieved, the Xe lamp and the peristaltic pump that delivers the H<sub>2</sub>O<sub>2</sub> solution were turned on. Fig. 8 shows the variation of the conversion (%) of NO with irradiation time. It was obvious that the NO conversion gradually rose with the increase of irradiation time and then reached a steady state for all the samples. In this experiment, the steady state was defined as the situation that the variation of the outlet concentration of the NO was less than 5%. However, as the reaction progressed, oxidation products would continue to accumulate on the surface of ms-BiVO<sub>4</sub> sample, it is inferred that the NO conversion might have dropped if the reaction were adequately prolonged with the irradiation time. Based on the PCO of NO within 150 min under visible light irradiation, the photocatalytic efficiency order of the various hierarchical ms-BiVO<sub>4</sub> samples could be obtained as follows: ms-BiVO<sub>4</sub> (pH = 8, 48.5%) > ms-BiVO<sub>4</sub> (pH = 9, 41.5%) > ms-BiVO<sub>4</sub> (pH = 10, 33.6%). As a reference, four preliminary experiments with the absence of the ms-BiVO<sub>4</sub> photocatalyst (pH = 8), visible-light irradiation, the H<sub>2</sub>O<sub>2</sub> solution, both ms-BiVO<sub>4</sub> sample (pH = 8) and the H<sub>2</sub>O<sub>2</sub> solution, respectively, were conducted. As shown in Fig. S2, corresponding NO oxidation ratios were only 6.7%, 8.0%, 5.6% and 2.8%, illustrating that NO could hardly be oxidized without ms-BiVO<sub>4</sub>, visible-light irradiation and the H<sub>2</sub>O<sub>2</sub> solution, or be photolyzed by mere visible-light irradiation. Therefore, the photocatalytic performance of ms-BiVO<sub>4</sub> with the flower-like structure was superior to the half-open flower-like and tubular shape. The high photoactivity of ms-BiVO<sub>4</sub> samples could be related to the difference of their special surface structure and the special surface areas. The specific surface area of synthesized ms-BiVO<sub>4</sub> powders at different pH values was listed in Table 1. It could be clearly seen that the specific surface area did not play a leading role in the photocatalytic performance.

Therefore, the enhanced photocatalytic performance of flower-like structured ms-BiVO<sub>4</sub> was more directly related to its highly active surface structures with preferential exposed (040) facet and its good crystallinity. The result was accordance with those previous reports.<sup>32,6</sup> Li and co-workers considered that the ms-BiVO<sub>4</sub> with more exposed (040) facet provided more multi-atomic centers BiV<sub>4</sub>, which would be the origin of the multi-electron transfer for O<sub>2</sub> evolution. And Kudo et al. held that good crystallinity of the photocatastre remains a major factor in determining the high photoactivity.

Ion Chromatography (IC) was used to further confirm the composition of reaction products of the PCO of gaseous NO in the presence of ms-BiVO<sub>4</sub> photocatalysts under VL irradiation, as well as to clarify the dispersion of oxidation products accumulated on the surface of photocatalysts and collected in the volumetric flask. After an experiment was completely conducted, the photocatalyst was immersed in 9 mL deionized water for 120 min in order that ions on the surface of the photocatalyst after reaction could intensively dissolve into the solution. After the clear supernatant was obtained by centrifugation (5000 rpm, 5 min), 1 mL solution was taken out, diluted with deionized water in the ratio of 1 : 10. Simultaneously, 1 mL solution was removed from the collected solution (~ 6 mL) in volumetric flak, diluted by a factor of 400. Then the above two groups of diluted solution were injected into the IC. The result of qualitative analysis, taking ms-BiVO<sub>4</sub> (pH 8) for an instance, is shown in Fig. 8b, which demonstrated that NO<sub>3</sub><sup>-</sup> existed in the solution. In addition, standard solutions were prepared and corresponding IC were conducted, of which the fitting line is displayed in Fig.S3. Therefore, the concentration of NO<sub>3</sub><sup>-</sup> could be acquired by external standard method, which is shown in Table 1. With the increase of pH values of precursor solution, the NO<sub>3</sub><sup>-</sup> accumulation on the surface of photocatalyst gradually increased. It illustrated that the NO<sub>3</sub><sup>-</sup> accumulated on the booming flower-like structured ms-BiVO<sub>4</sub> (pH 8) sample was more easily flushed by H<sub>2</sub>O<sub>2</sub> solution. Then the exposed (040) plane was less covered by the products and the high photoactivity was achieved for a long time. Fig. 8c shows a durability of photocatalytic performance of ms-BiVO<sub>4</sub> (pH 8) in the PCO

of NO under VL irradiation for 2000 min. It could be clearly seen that the photoactivity did not exhibit a significant loss. Therefore, the unique morphology of synthesized ms-BiVO<sub>4</sub> samples had an impact on the dispersion of the oxidation products accumulated on the surface of photocatalysts and collected in the volumetric flask, which would further influence on the photoactivity.

**(Figure 8)**

Additionally, we did not find the existence of NO<sub>2</sub> when we analyzed the gas products (every 10 min reaction) by the Ecom-JZKN flue gas analyzer. It could be obtained that NO<sub>3</sub><sup>-</sup> was the major reaction product in the PCO of NO process. Subsequently, we carried out a trapping experiment to intuitively understand the involvement of active radical species in the PCO of NO process under VL irradiation over the ms-BiVO<sub>4</sub> photocatalysts, taking ms-BiVO<sub>4</sub> (pH 8) for an instance, which was displayed in Fig. 9. Five quartz tubes filled with 40 mL deionized water and 4 mL 30% H<sub>2</sub>O<sub>2</sub> solution were divided into four experimental groups (a, b, c, d) and the control group (e). Furthermore, 10 mg ms-BiVO<sub>4</sub> (pH 8) was put into each experimental group, respectively. Subsequently, 1 mL isopropyl alcohol (IPA) was injected into group (b) in order that hydroxyl radicals (·OH) could be quenched, 0.1 mmol p-benzoquinone (BQ) was dispersed into group (c) as the scavenger of superoxide radicals (·O<sub>2</sub><sup>-</sup>) and 0.1 mmol ammonium oxalate (AO) as holes (h<sup>+</sup>) scavenger was added into group (d).<sup>33</sup> Then NO was introduced through the gas distributor and all quartz tubes were exposed to VL irradiation in stirring condition for 30 min. After the clear supernatant was obtained by centrifugation (5000 rpm, 5 min) and then injected into IC. Quantitative analysis shows that concentrations of NO<sub>3</sub><sup>-</sup> in solutions of the experimental group (a), (b), (c) and (d) as well as the control group (e) are 19.63, 7.26, 10.62, 15.56 and 4.63 mg·L<sup>-1</sup>, respectively. It could be seen that ·OH, ·O<sub>2</sub><sup>-</sup> and h<sup>+</sup> are the important and efficient active species in the PCO of NO. Since the concentration of NO<sub>3</sub><sup>-</sup> in the solutions of group (b), free from the effect of ·OH, was the lowest among all experimental groups and only a bit higher than that in the solution of the control group, it was evident that ·OH played a pivotal role in the

PCO of NO. In order to further validate the  $\cdot\text{OH}$  formed on the surface of ms-BiVO<sub>4</sub> sample, the photoluminescence (PL) technique using terephthalic acid as a probe molecule was applied. Fig. 10 shows the PL spectra of the control group and the experimental group (Part 2.3) under the 120 min VL irradiation. Obviously, the PL intensity of experimental group at about 426 nm was higher than that of the control group, which illustrated that a large amount of  $\cdot\text{OH}$  was produced in the presence of the ms-BiVO<sub>4</sub> photocatalyst.

**(Figure 9)**

**(Figure 10)**

#### 4 Conclusions

In summary, we successfully synthesized 3D ms-BiVO<sub>4</sub> superstructure with diverse morphologies by facile pH-dictated solvothermal routes under alkaline conditions with the aid of NH<sub>3</sub>·H<sub>2</sub>O. The prepared 3D ms-BiVO<sub>4</sub> superstructure was flower-like (pH 8), double-layer half-open flower-like (pH 9) and hollow tube with square cross-sections (pH 10), respectively. In this paper it was evident that morphology, surface structure and crystallinity of ms-BiVO<sub>4</sub> prepared under different pH conditions were important to their photoactivity. The good crystallinity and preferred (040) facet of the flower-like ms-BiVO<sub>4</sub> led to an enhancement for the VL-induced PCO of NO. Furthermore, the unique morphology had an impact on the dispersion of the oxidation products accumulated on the surface of photocatalysts and flushed into the volumetric flask, which further influence the photocatalytic performance. The effects of the active species involved in the photocatalytic process were also examined. The present results indicated that controllable designed materials with predictable morphology and exposed plane might bring new opportunities for developing highly visible-light-active semiconductor photocatalysts.

#### Acknowledgements

This work was financially supported by the Assembly Foundation of The Industry and Information Ministry of

the People's Republic of China 2012 (543), the National Natural Science Foundation of China (51408309), Science and Technology Support Program of Jiangsu Province (BE2014713), Natural Science Foundation of Jiangsu Province (BK20140777), Scientific Research Project of Environmental Protection Department of Jiangsu Province (2013003), Industry-Academia Cooperation Innovation Fund Projects of Jiangsu Province (BY2014004-10), Science and Technology Project of Nanjing (201306012), the Priority Academic Program Development of Jiangsu Higher Education Institutions.

## References

- 1 R. Li, F. X. Zhang, D. Wang, J. X. Yang, M. G. Li, J. Zhu, X. Zhou, H. X. Han and C. Li, *Nat. Commun.*, 2013, **4**, 1432.
- 2 S. Obregón and G. Colón, *J. Mol. Catal. A: Chem.*, 2013, **376**, 40.
- 3 Z. H. Ai, W. Ho, S. C. Lee and L. Z. Zhang, *Environ. Sci. Technol.*, 2009, **43**, 4143.
- 4 G. C. Xi and J. H. Ye, *ChemComm.*, 2010, **46**, 1893.
- 5 Y. Huang, Z. H. Ai, W. Ho, M. J. Chen and S. C. Lee, *J. Phys. Chem. C*, 2010, **114**, 6342.
- 6 J. Yu and A. Kudo, *Adv. Funct. Materials.*, 2006, **16**, 2163.
- 7 M. L. Guan, D. K. Ma, S. W. Hu, Y. J. Chen and S. M. Huang, *Inorg. Chem.*, 2011, **50**, 800.
- 8 M. Ou, Q. Zhong and S. L. Zhang, *J Sol-Gel Sci Technol*, 2014, **72**, 443.
- 9 T. W. Kim and K. S. Choi, *Science*, 2014, **343**, 990.
- 10 M. Long, W. M. Cai; J. Cai,; B. X. Zhou, X. Y. Chai and Y. H. Wu, *J. Phys. Chem. B*, 2006, **110**, 20211.
- 11 W. Wang, X. Huang, S. Wu, Y. Zhou, L. Wang, H. Shi, Y. Liang and B. Zou, *Appl. Catal. B: Environ.*, 2013, **134-135**, 293.
- 12 Y. Hu, D. Li, Y. Zheng, W. Chen, Y. He, Y. Shao, X. Fu and G. Xiao, *Appl. Catal. B: Environ.*, 2011, **104**, 30.
- 13 Z. H. Ai and S. C. Lee, *Appl. Surf. Sci.*, 2013, **280**, 354.

- 14 H. M. Fan, T. F. Jiang, H. Y. Li, D. J. Wang, L. L. Wang, J. L. Zhai, D. Q. He, P. Wang and T. F. Xie, *J. Phys. Chem. C*, 2012, **116**, 2425.
- 15 X. Zhang, Z. H. Ai, F. L. Jia, L. Z. Zhang, X. X. Fan and Z. G. Zou, *Mater. Chem. Phys.*, 2007, **103**, 162.
- 16 S. Y. Dong, J. L. Feng, Y. K. Li, L. M. Hu, M. L. Liu, Y. F. Wang, Y. Q. Pi, J. Y. Sun and J. H. Sun, *Appl. Catal. B: Environ.*, 2014, **152-153**, 413.
- 17 D. Wang, H. F. Jiang, X. Zong, Q. Xu, Y. Ma, G. L. Li and C. Li, *Chem. Eur. J.*, 2011, **17**, 1275.
- 18 M. Ge, L. Liu, W. Chen and Z. Zhou, *CrystEngComm*, 2012, **14**, 1038.
- 19 L. Ren, L. L. Ma, L. Jin, J. B. Wang, M. Q. Qiu and Y. Yu, *Nanotechnology*, 2009, **20**, 405602.
- 20 S. Tokunaga, H. Kato and A. Kudo, *Chem. Mater.*, 2001, **13**, 4624.
- 21 G. Q. Tan, L. L. Zhang, H. J. Ren, S. S. Wei, J. Huang and A. Xia, *ACS appl. Mater. Interfaces*, 2013, **5**, 5186.
- 22 L. Zhou, W. Z. Wang, L. S. Zhang, H. L. Xu and W. Zhu, *J. Phys. Chem. C*, 2007, **111**, 13659.
- 23 L. Zhou, W. Z. Wang and H. L. Xu, *Cryst Growth Des*, 2008, **8**, 728.
- 24 S. Obregón, A. Caballero and G. Colón, *Appl. Catal. B: Environ.*, 2012, **117-118**, 59.
- 25 Z. J. Zhou, M. Long, W. M. Cai and J. Cai, *J. Mol. Catal. A: Chem.*, 2012, **353-354**, 22.
- 26 G. S. Li, D. Q. Zhang and J. C. Yu, *Chem. Mater.*, 2008, **20**, 3983.
- 27 M. Wang, Q. Liu, Y. S. Che, L. F. Zhag and D. Zhang, *J. Alloys. Compd.*, 2013, **548**, 70.
- 28 P. Madhusudan, J. R. Ran, J. Zhang, J. G. Yu and G. Liu, *Appl. Catal. B: Environ.*, 2011, **110**, 286.
- 29 K. Yu, S. G. Yang, S. A. Boyd, H. Z. Chen and C. Sun, *J. hazard. mater.*, 2011, **197**, 88.
- 30 L. Zhou, W. Z. Wang, S. W. Liu, L. S. Zhang, H. L. Xu and W. Zhu, *J. Mol. Catal A: Chem.*, 2006, **252**, 120.
- 31 Z. B. Wu, Z. Y. Sheng, Y. Liu, H. Q. Wang, N. Tang and J. Wang, *J. hazard. mater.*, 2009, **164**, 542.
- 32 S. M. Thalluri, M. Hussain, G. Saracco, J. Barber and N. Russo, *Ind. Eng. Chem. Res.*, 2014, **53**, 2640.

**Table Captions**

**Table 1** The morphology, surface and structural characterization, and the results of Ion Chromatography quantitative analysis for different ms-BiVO<sub>4</sub> samples.

Sample	Morphology	$I_{(040)}/I_{(121)}$	$I_{(110)}/I_{(121)}$	$I_{(002)}/I_{(121)}$	BET ( $\text{m}^2/\text{g}$ )	Eg (eV)	IC-400 (mg/L)	IC-90 (mg/L)
pH = 8	flower	0.355	0.269	0.176	0.78	2.44	40.06	9.93
pH = 9	double-layer	0.096	0.314	0.290	3.32	2.45	19.73	29.36
	half-open flower							
pH = 10	hollow tube with	0.073	0.390	0.640	0.58	2.48	13.58	31.50
	square cross-sections							

**Table 1** The morphology, surface and structural characterization, and the results of Ion Chromatography quantitative analysis for different  $\text{ms-BiVO}_4$  samples.

IC-400: the  $\text{NO}_3^-$  concentration in the collected solution in volumetric flask which was diluted by a factor of 400.

IC-90: the  $\text{NO}_3^-$  concentration washed from the surface of the photocatalyst which was diluted by a factor of 9 \* 10.

## Figure Captions

**Fig. 1** Schematic diagram of the experimental apparatus for photocatalytic oxidation of NO.

**Fig. 2** XRD patterns of BiVO<sub>4</sub> powders by solvothermal method at different pH values: at acidic or neutral condition (pH = 2 or 7) (a) and at alkaline condition (pH = 8, 9 and 10) (b).

**Fig. 3** SEM images of as-synthesized ms-BiVO<sub>4</sub> powders at different pH values: pH = 8 (a<sub>1</sub>-a<sub>3</sub>); pH = 9 (b<sub>1</sub>, b<sub>2</sub>) and pH = 10 (c<sub>1</sub>, c<sub>2</sub>).

**Fig. 4** Schematic illustration of the proposed formation mechanism of flower-like ms-BiVO<sub>4</sub> superstructure.

**Fig. 5** TEM images of ms-BiVO<sub>4</sub> samples synthesized at different pH values (a<sub>1</sub>, b<sub>1</sub>, c<sub>1</sub>) and the corresponding HRTEM and SAED (inset) taken from the edge, as labeled in TEM images (a<sub>2</sub>, b<sub>2</sub>, c<sub>2</sub>).

**Fig. 6** UV-vis diffuse reflection spectra patterns (a) and plots of  $(\alpha h\nu)^2$  versus  $h\nu$  (b) of the as-synthesized ms-BiVO<sub>4</sub> powders at different pH values.

**Fig. 7** Comparison of XPS high-resolution scans over Bi 4f (a), V 2p (b) and O1s (c) peaks on ms-BiVO<sub>4</sub> (pH 8) in the dark overnight (I), under visible light irradiation for 30 min (II) and after the end of 150 min PCO of NO experiment (III).

**Fig. 8** Variations of NO conversion efficiency with irradiation time for the as-synthesized ms-BiVO<sub>4</sub> samples at different pH values (a); Ion Chromatography analysis of reaction products after the photocatalytic reaction in the presence of ms-BiVO<sub>4</sub> (pH 8) for 150 min (b) and the durability test over ms-BiVO<sub>4</sub> (pH 8) in the PCO of NO under VL irradiation for 2000 min (c).

**Fig. 9** Schematic illustration of experimental groups (a, b, c, d) and the control group (e) in the trapping experiment.

**Fig. 10** Fluorescence spectra of TAOH solutions generated by the experimental group with ms-BiVO<sub>4</sub> (pH 8) and the control group under visible-light irradiation.

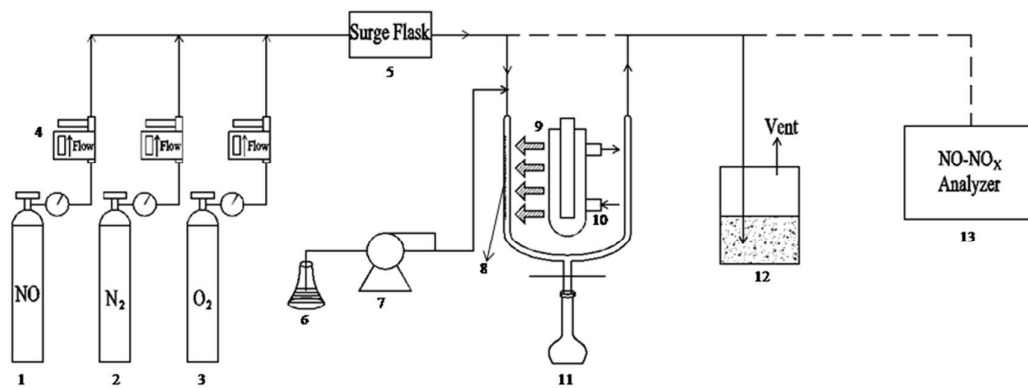


**Fig. 1** Schematic diagram of the experimental apparatus for photocatalytic oxidation of NO. 1 - NO; 2 - N<sub>2</sub>; 3 - O<sub>2</sub>; 4 - mass flowmeter; 5 - surge flask; 6 - 30% H<sub>2</sub>O<sub>2</sub> solution; 7 - peristaltic pump; 8 - quartz photoreactor; 9 - light source; 10 - condensate water; 11 - 10 mL volumetric flask; 12 - wet scrubber; 13 - NO-NO<sub>x</sub> analyzer.

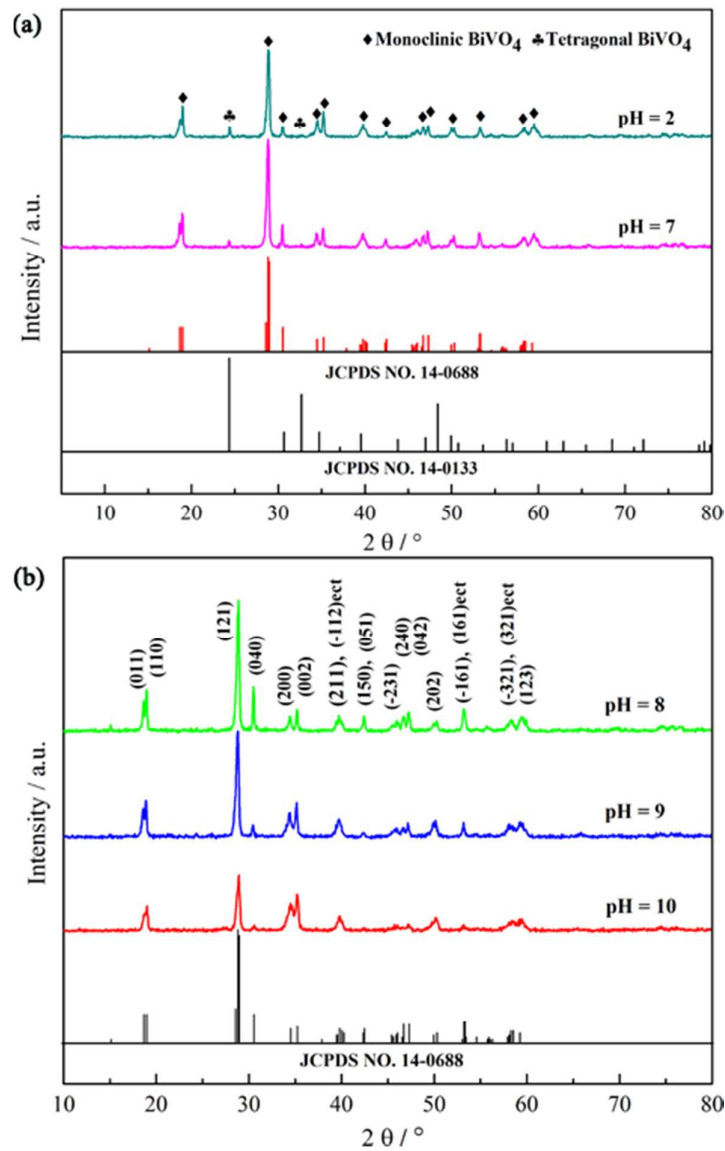


**Fig. 2** XRD patterns of  $\text{BiVO}_4$  powders by solvothermal method at different pH values: at acidic or neutral condition (pH = 2 or 7) (a) and at alkaline condition (pH = 8, 9 and 10) (b).

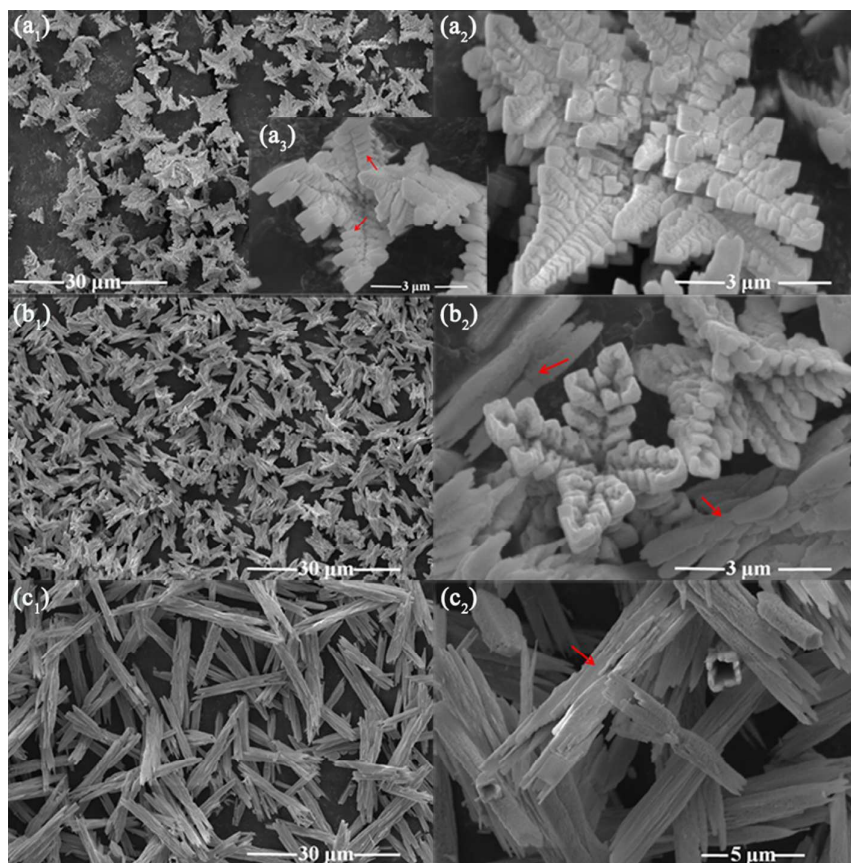


Fig. 3 SEM images of as-synthesized ms-BiVO<sub>4</sub> powders at different pH values: pH = 8 (a<sub>1</sub>-a<sub>3</sub>); pH = 9 (b<sub>1</sub>, b<sub>2</sub>) and pH = 10 (c<sub>1</sub>, c<sub>2</sub>).

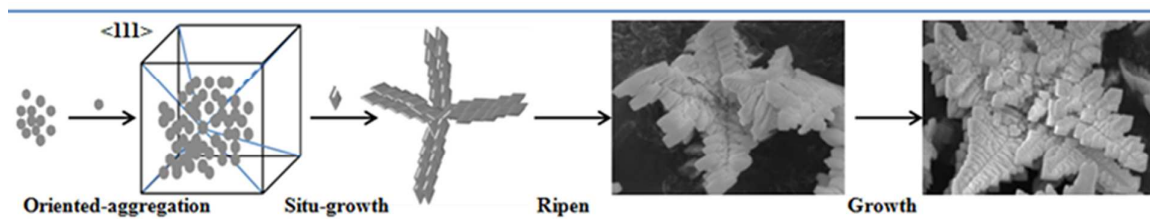


Fig. 4 Schematic illustration of the proposed formation mechanism of flower-like ms-BiVO<sub>4</sub> superstructure.

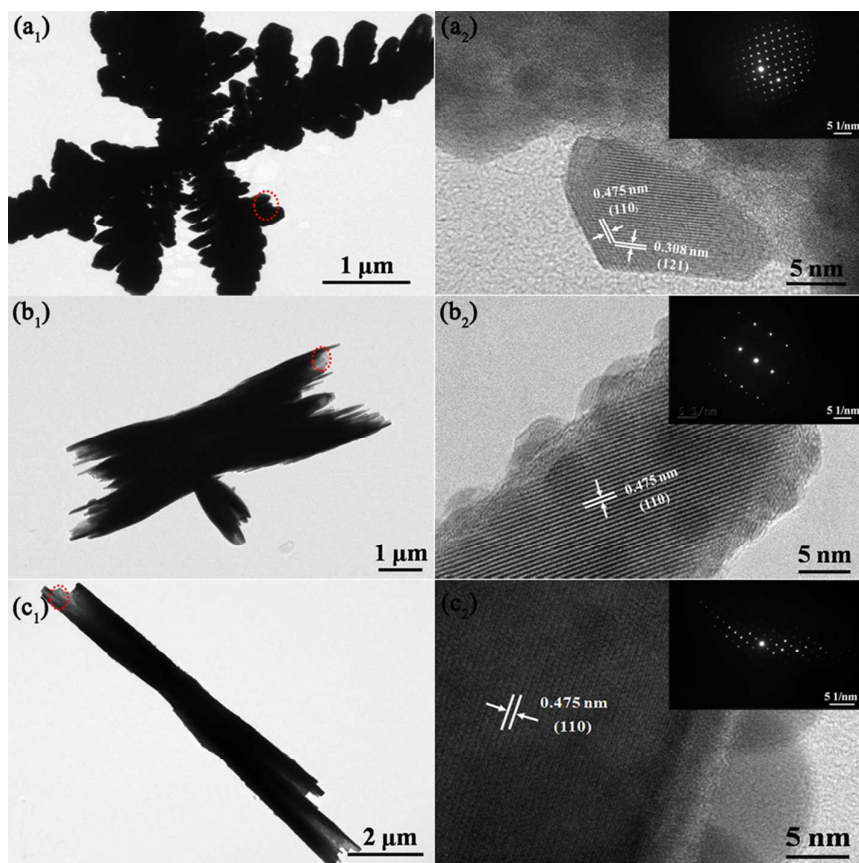


Fig. 5 TEM images of ms-BiVO<sub>4</sub> samples synthesized at different pH values (a<sub>1</sub>, b<sub>1</sub>, c<sub>1</sub>) and the corresponding HRTEM and SAED (inset) taken from the edge, as labeled in TEM images (a<sub>2</sub>, b<sub>2</sub>, c<sub>2</sub>).

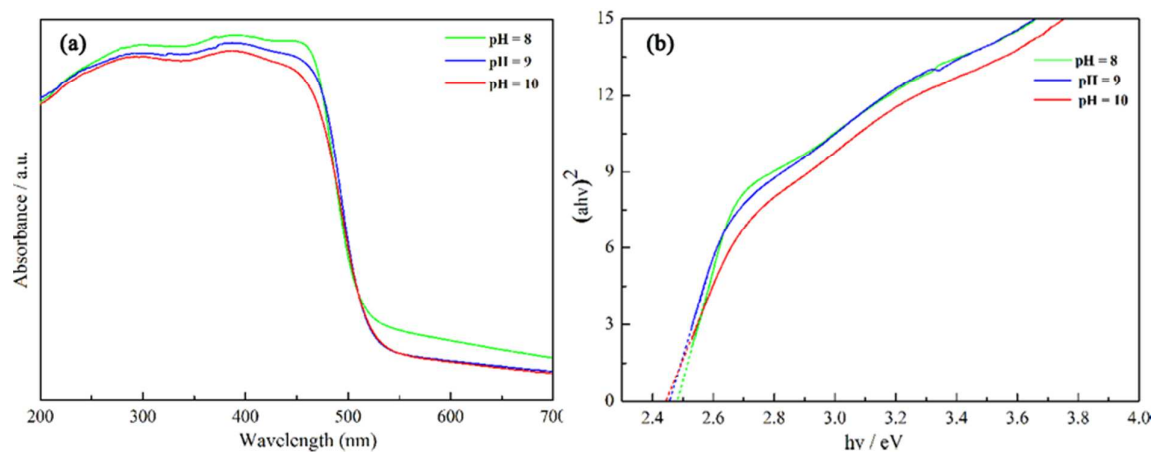
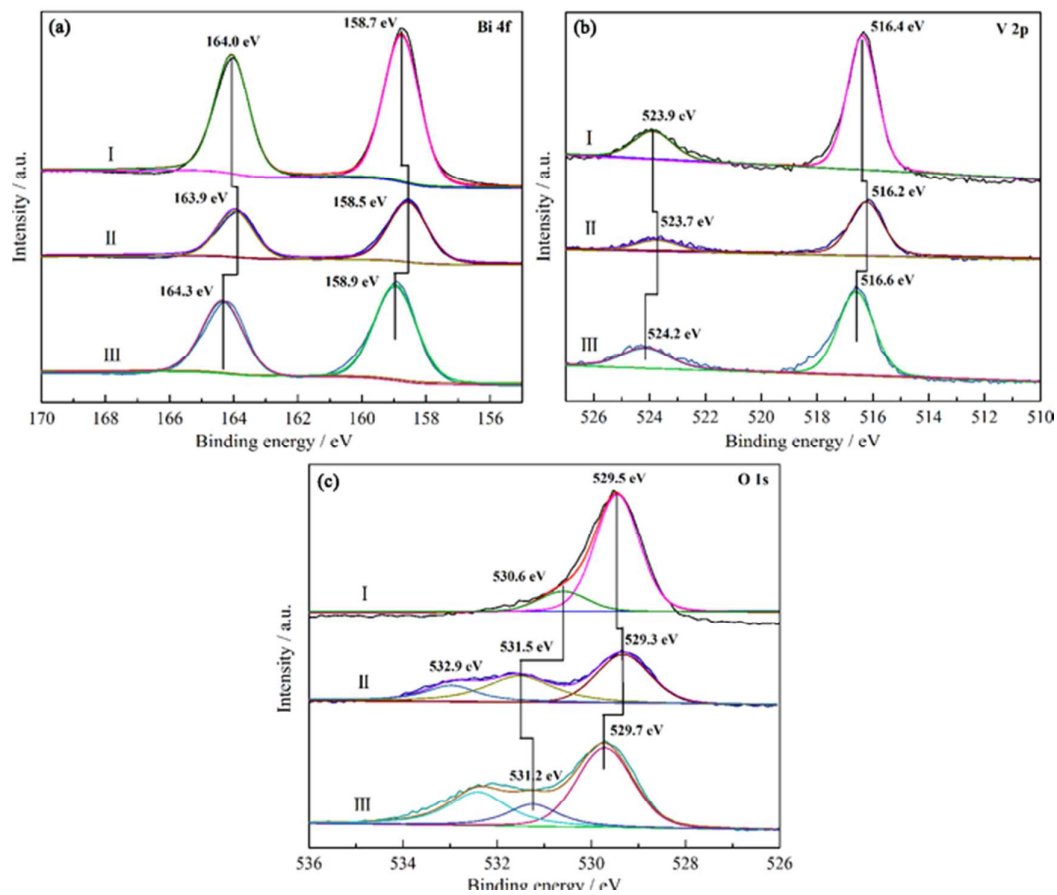
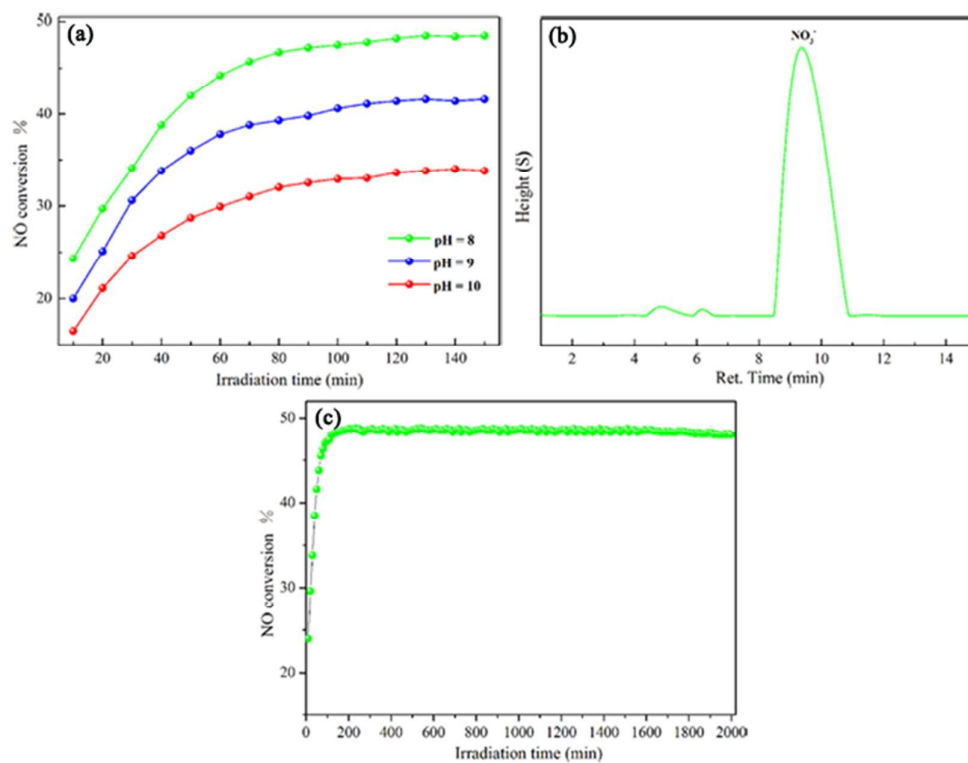


Fig. 6 UV-vis diffuse reflection spectra patterns (a) and plots of  $(\alpha hv)^2$  versus  $h\nu$  (b) of the as-synthesized ms-BiVO<sub>4</sub> powders at different pH values.



**Fig. 7** Comparison of XPS high-resolution scans over Bi 4f (a), V 2p (b) and O1s (c) peaks on ms-BiVO<sub>4</sub> (pH 8) in the dark overnight (I), under visible light irradiation for 30 min (II) and after the end of 150 min PCO of NO experiment (III).



**Fig. 8** Variations of NO conversion efficiency with irradiation time for the as-synthesized ms-BiVO<sub>4</sub> samples at different pH values (a); Ion Chromatography analysis of reaction products after the photocatalytic reaction in the presence of ms-BiVO<sub>4</sub> (pH 8) for 150 min (b) and the durability test over ms-BiVO<sub>4</sub> (pH 8) in the PCO of NO under VL irradiation for 2000 min (c).

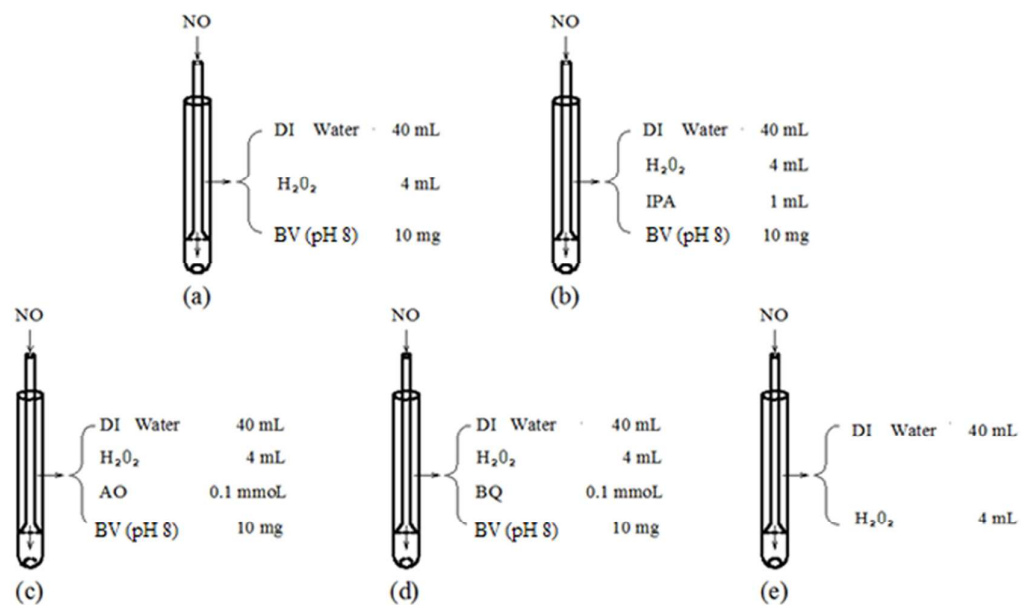


**Fig. 9** Schematic illustration of experimental groups (a, b, c, d) and the control group (e) in the trapping experiment.

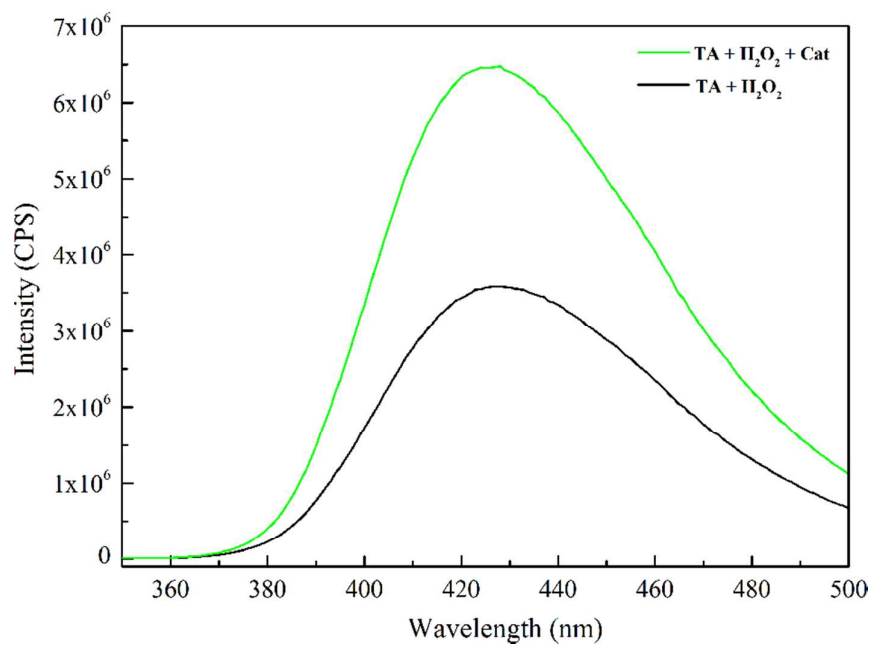


**Fig. 10** Fluorescence spectra of TAOH solutions generated by the experimental group with  $\text{ms-BiVO}_4$  (pH 8) and the control group under visible-light irradiation.